Journal of Magnetic Resonance 346 (2023) 107342

Contents lists available at ScienceDirect

Journal of Magnetic Resonance

journal homepage: www.elsevier.com/locate/jmr

NMR spectrum reconstruction as a pattern recognition problem

Amir Jahangiri [a], Xiao Han [b], Dmitry Lesovoy [c], Tatiana Agback [d], Peter Agback [d], Adnane Achour [b], Vladislav Orekhov [a,*]

[a] Department of Chemistry and Molecular Biology, Swedish NMR Centre, University of Gothenburg, Box 465, Gothenburg 40530, Sweden
[b] Science for Life Laboratory, Department of Medicine, Karolinska Institute, and Division of Infectious Diseases, Karolinska University Hospital, Stockholm 17176, Sweden
[c] Shemyakin-Ovchinnikov Institute of Bioorganic Chemistry RA, Moscow 117997, Russia
[d] Department of Molecular Sciences, Swedish University of Agricultural Sciences, Box 7015, Uppsala 75007, Sweden

ARTICLE INFO

Article history:
Received 13 September 2022
Revised 15 November 2022
Accepted 19 November 2022
Available online 24 November 2022

Keywords:
Nuclear magnetic resonance
Non-uniform sampling
DNN
CNN
Wave-net

ABSTRACT

A new deep neural network based on the WaveNet architecture (WNN) is presented, which is designed to grasp specific patterns in the NMR spectra. When trained at a fixed non-uniform sampling (NUS) schedule, the WNN benefits from pattern recognition of the corresponding point spread function (PSF) pattern produced by each spectral peak resulting in the highest quality and robust reconstruction of the NUS spectra as demonstrated in simulations and exemplified in this work on 2D ^{1}H-^{15}N correlation spectra of three representative globular proteins with different sizes: Ubiquitin (8.6 kDa), Azurin (14 kDa), and Malt1 (44 kDa). The pattern recognition by WNN is also demonstrated for successful virtual homodecoupling in a 2D methyl ^{1}H-^{13}C — HMQC spectrum of MALT1. We demonstrate using WNN that prior knowledge about the NUS schedule, which so far was not been fully exploited, can be used for designing new powerful NMR processing techniques that surpass the existing algorithmic methods.

1. Introduction

NMR spectroscopy is an analytical technique that provides atomic-level information about molecular structure, dynamics, and interactions [1,2]. Since the invention of Fourier NMR in 1970's, modern spectra have been acquired by sampling the signal in the time domain. This not only significantly improved sensitivity but also enabled rapid development of multidimensional NMR experiments that offer ultimate resolution and rich information content. However, an increase in resolution and dimensionality leads to very long measurement time needed to systematically uniformly sample (US) large volume of the multidimensional data set [3]. To address this problem, experimental time is saved by not measuring the major fraction of the US data in the widely used approach called non-uniform sampling (NUS). Since Fourier transform can no longer produce high quality spectra reconstruction from the NUS data, many alternative signal processing techniques were developed in the past years [3–15]. Reconstruction of a spectrum from NUS, *i.e.* incomplete data, is an ill-defined mathematical problem which can only be solved by introducing prior assumptions about the spectrum and/or the signal in the time domain. For example, in the approach known as Compressed Sensing, the most sparse spectrum is selected [6]. Generally, the more we constrain the solution with correct assumptions, the better is reconstruction quality and the less NUS data are needed. Until recently, the progress in the NUS spectra processing focused on solving two practical tasks, specifically to *i)* define the best prior assumptions and *ii)* design computationally effective algorithms for their implementation.

Artificial Intelligence (AI) - specifically Deep learning (DL) - has a potential to solve both the above-mentioned tasks in a new and efficient way. Although the first demonstrations of the machine learning applications in NMR can be traced back to the 1970s [16], practical applications could not be developed until reaching the modern level of algorithms and computer hardware. Over the last years, DL has led to impressive advances in many fields, including NMR spectroscopy [17]. For example, DL has a marked ability for the spectra denoising [18], prediction of chemical shift [19], automated peak picking [20,21] and structure calculation from NMR spectra [22], as well as for fast and high-quality NMR reconstruction of NUS spectra [23–26]. The distinctive feature of DL neural networks (DNNs) is their ability to establish essential correlations between the input and output and thus to retrieve relevant multi-facet prior information, *e.g.* about NMR signal, that is difficult to formulate in an analytical form and embed into a computer algorithm. Although a trained DNN is usually considered as a

* Corresponding author.
E-mail address: vladislav.orekhov@nmr.gu.se (V. Orekhov).

https://doi.org/10.1016/j.jmr.2022.107342
1090-7807/

black box, there are reports, where the knowledge mined by the network in the training process was rationalized and even reverse-engineered [27]. In this work, we learned from the DNN that the NUS schedule is also a valuable and so far not fully exploited source of prior information for the spectrum reconstruction. DNNs are generally very efficient in pattern recognition [28]. In NMR, DNNs were successfully used for automated peak picking [21] and virtual homo-nuclear decoupling [29]. In this work, we note that a very distinct pattern of spectral aliasing artifacts corresponding to a particular sampling schedule can be effectively recognized and rectified by DNN. In this study, we develop and train new deep neural networks to solve the NUS reconstruction problem. We call our software tool – WNN as it is inspired by WaveNet DNN architecture which was originally conceived as a model for raw audio signal [30]. The broad reception field featured by the WaveNet DNNs is particularly important for grasping the entire pattern of NUS-associated aliasing artifacts, which spread over the entire spectrum area.

Here, after a description of the network architecture and synthetic data used for the training, we compared performance of different reconstruction protocols for representative two-dimensional NUS spectra of three globular proteins of different sizes. The five reconstruction protocols include Compressed Sensing Iterative Soft Thresholding algorithm (CS-IST) [6] and Sparse Multidimensional Iterative Lineshape-Enhanced algorithm (SMILE) [15] as two representative traditional methods, as well as three WNNs differing in data sets used for their training. Specifically, WNN-F trained on a fixed, *i.e.* the same NUS schedule for all training spectra, WNN-P and WNN-R trained on different NUS tables from Poisson-gap and flat-random distribution, respectively. Finally, as another demonstration of the pattern recognition by WNN, we present the virtual decoupling on the example of a methyl ^{1}H-^{13}C — HMQC spectrum in the 44 kDa protein MALT1 [31,32].

2. Materials and methods

2.1. Synthetic data for training and testing

2.1.1. Data model

Obtaining a very large experimental data set needed for the DNN training is a challenge. As an alternative, it is common to use easily generated synthetic data as a good proxy for realistic experimental NMR spectra. In many practical applications NMR time domain signal X_{FID}, usually called free induction decay (FID), can be presented as a superposition of a small number of exponential functions:

$$X_{FID}(t_1) = \sum_n a_n e^{-t_1/\tau_n} e^{i(2\pi\omega_n t_1 + \phi_n)} cos(\pi J_n t_1) + noise \quad (1)$$

where n runs over the number of exponentials, and the nth exponential has the amplitude a_n, phase ϕ_n, relaxation time τ_n, and frequency ω_n. In addition, in the present work, we added a scalar coupling with constant J_n. Time t_1 is given by multiplication of the dwell time (DW) and series 0, 1, …, N-1, which enumerates the sampled time points in the FID. The total acquisition time (AT) is given by product ($N \times DW$). Also, we added the Gaussian *noise* to emulate the noise presented in realistic NMR spectra. The desired number of different FIDs for the training set is easily simulated by varying the above parameters. The parameters and their ranges used for generating the synthetic data are summarized in Table 1.

The uniformly sampling spectrum is obtained by:

$$S_{FID} = DFT(X_{FID}) \quad (2)$$

Table 1
Parameters for the synthetic FID.

	NUS reconstruction	Virtual decoupling
$a_n \in \mathbb{R}$	0.05–1	0.05–1
$\omega_n \in \mathbb{R}$	0.1–0.9	0.1–0.9
$\tau_n \in \mathbb{R}$	$0.5AT$ - $5AT$	$0.25AT$ - $0.5AT$
$\phi_n \in \mathbb{R}$	-5° - 5°	-5° - 5°
$J_n \in \mathbb{R}$	0	$27Hz$ - $45Hz$
$N \in \mathbb{N}$	128	256
$n \in \mathbb{Z}$	0–30	0–15
$noise \in \mathbb{C}$	0–0.01*	0–0.01*

* The absolute value of a complex number.

where $DFT()$ is the discrete Fourier transform.

Then, the Non-Uniform Sampling (NUS) signal, Y, is generated from X_{FID} as:

$$Y = u \circ X_{FID} \quad (3)$$

where $\circ$ is Hadamard product and u is the NUS schedule in a vector the representation with ones and zeros at the acquired and non-acquired positions in X_{FID}, respectively.

Using the Fourier convolution theorem, the NUS spectrum, $S_{NUS} = DFT(Y)$ is:

$$\begin{aligned} S_{NUS} &= DFT(u \circ X_{FID}) \\ &= DFT(u) * DFT(X_{FID}) \\ &= U * S_{FID} \end{aligned} \quad (4)$$

where $U = DFT(u)$ is the Point Spread Function (PSF) and $*$ is convolution. Because of the convolution of U and S_{FID}, each signal in the spectrum generates a unique pattern of random-noise-like artifacts, which is defined by the specific NUS schedule. Note that since function u is real, PSF is symmetric around the true peak position.

In the case of 2D spectra used in this work, the NUS and above-described model Eqs. (1)–(4) are applied only to the indirectly detected spectral dimension referred to as the first with time variable t_1. The second, direct dimension, is usually acquired in full and Fourier transformed. Thus, slices corresponding to the adjacent ω_2 points may share the same signals in t_1 dimension. To take this into account, we use the sliding window approach, which can also be found in the FID-Net architecture [25] and is used in the Multi-Dimensional Decomposition for general N-dimensional case [33]. For three points in the window, Eq. (1) applies with the same parameters except for the amplitude a_n. Since we assume the peaks in the direct dimension as Lorentzian lines, the amplitude a_n^k of exponent n in slice k is:

$$a_n^k = \frac{\lambda^2}{\lambda^2 + (k\Delta\omega_2)^2} \quad (5)$$

where $\Delta\omega_2$ is the spectrum digital resolution for the directly detected dimension ω_2. λ is the line width, which is randomly selected in the range $\Delta\omega_2 < \lambda < 5\Delta\omega_2$. Then, k runs over three consecutive integer numbers resulting in $0.05 \leqslant a_n^k \leqslant 1$.

2.1.2. Training WNN with different NUS-PSF strategies

When generating data sets for training the WNNs, we used three strategies: (i) Fixed (WNN-F), where the same NUS schedule of the Poisson-gap type [9] was used for all K spectra in the training set, (ii) unfixed Poisson-gap (WNN-P), where each spectrum had individual Poisson-gap schedules, and (iii) unfixed random (WNN-R) with the individual NUS tables followed the flat random sampling distribution. Averaged NUS tables and PSFs for the three approaches are presented in Fig. 1. The implication of the different sampling schemes for the appearance of the PSF and for the outcome of the spectra reconstruction using traditional techniques

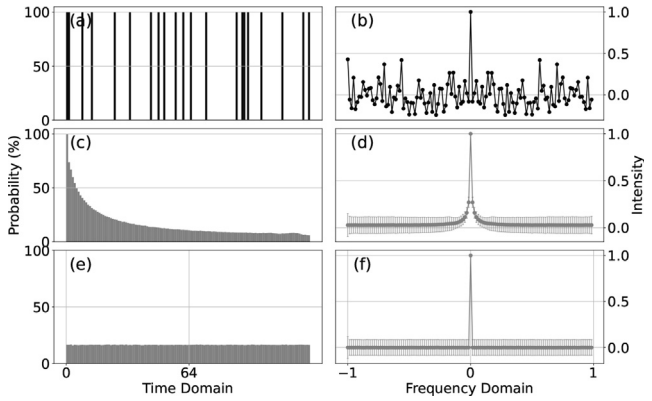

Fig. 1. The sampling scheme statistics. (a, c, e) - averaged percentage values for NUS schemes (21 points from the grid of 128) for 2^{16} different seeds. (b, d, f) - mean PSF values with standard deviations as the error bars. (a,b) fixed and (c, d) unfixed Poisson-gap NUS/PSF with $sin(\frac{\pi}{2}\frac{t}{t_{max}})$ modulation; and (e, f) NUS/PSF for unfixed random sampling.

have been previously discussed [34]. Specifically, the Poisson-gap schedules tend to push the aliasing artifacts away from the main peak and thus benefit spectra with clustered signals. The three approaches clearly differ in their PSF patterns, which can affect pattern recognition by the network. While WNN-F (Fig. 1b) has a distinct recognizable pattern, which is repeated for each true peak in the spectrum, WNN-R (Fig. 1f) has the most featureless average PSF, which is the least informative for the pattern recognition. WNN-P (Fig. 1d) with the visible featured slopes at the base of the central PSF peak takes position in between WNN-F and WNN-R.

Tables 1 and 2 present details of the training set parameters. In this work, we demonstrate WNN performance for several spectra of different complexity representing small, medium, and large proteins. For each of the three used proteins, we trained eleven WNN-F with eleven different Poisson-gap sampling schedules, one WNN-P, and one WNN-R. This gives in total 39 WNNs.

We also trained a WNN for the virtual decoupling (VD) in a methyl 2D ^{1}H-^{13}C — HMQC spectrum, where without the decoupling the ^{13}C resonances are split due to approximately 35 Hz J-coupling with the adjacent to the methyl ^{13}C atom. For the VD, the WNN, which contained only one DNN (Fig. 2b) and no correction step, was trained on uniform sampling data (see Section 2.2 for details).

2.1.3. Test synthetic data

In order to test trained WNNs, we generated synthetic data representing spectra for small, medium, and large proteins. For each

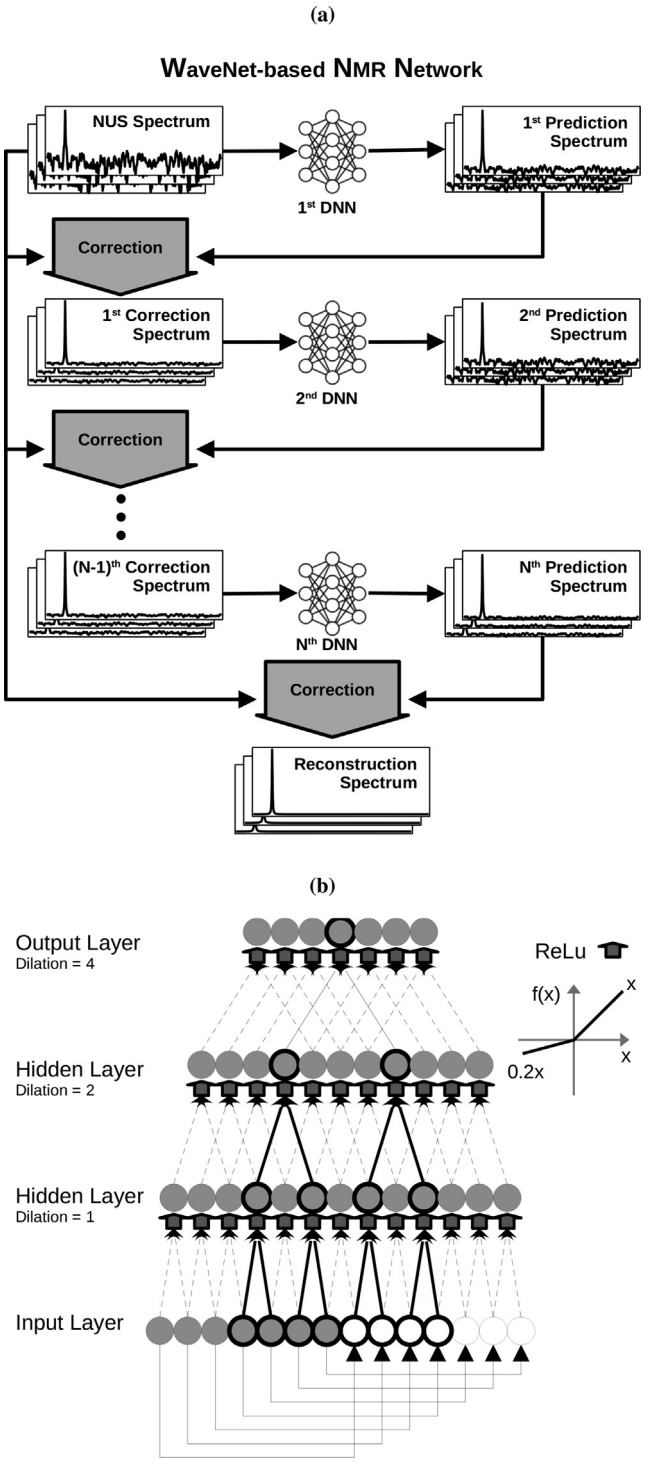

Fig. 2. a) WNN network architecture. b) Scheme of the DNN module used in WNN with $2^n - 1$ ($n \in \mathbb{N}$) points in the input layer, $n - 1$ hidden layers, 20 filters, and ReLU activation function between the layers.

Table 2
Training set parameters.

	NUS Reconstruction			VD
	Small	Medium	Large	
$K_{Training}$ [a]	2^{16}	2^{16}	2^{16}	2^{16}
n_{max} [b]	10	20	30	15×2
NUS rate	$\frac{11}{128}$	$\frac{21}{128}$	$\frac{31}{128}$	$\frac{256}{256}$
# of WNN-F	11	11	11	-
# of WNN-P	1	1	1	-
# of WNN-R	1	1	1	-
# of WNNs	**13**	**13**	**13**	**1**

[a] The number of spectra in the training set.
[b] The maximal number of peaks along indirect dimension.

Table 3
Testing set parameters.

	NUS Reconstruction			VD
	Small	Medium	Large	
$K_{Testing}$ [a]	1500	1500	1500	1500
n_{max}	10	20	30	15×2
NUS rate	$\frac{11}{128}$	$\frac{21}{128}$	$\frac{31}{128}$	$\frac{256}{256}$

[a] The number of spectra in the testing set.

case, the test data set contains 1500 uniform sampling synthetic 3-point sliding window spectra (Table 3): 1 (× 150) to 10 (× 150) peaks for a small protein, 1 (× 75) to 20 (× 75) peaks for a medium protein, and 1 (× 50) to 30 (× 50) peaks for a large protein. By using 11 NUS sampling schemes used for training 11 WNN-F for each protein size, 11 different NUS spectra for each protein size are simulated and then reconstructed.

2.2. WaveNet-based NMR Network (WNN) Architecture

In WNN, the entire network architecture consists of three main components: the DNNs, normalization, and the correction steps (Fig. 2).

2.2.1. A specific DNN architecture used in WNN

Schematics of the WNN are presented in Fig. 2. For the extraction of information about the PSF patterns within a NUS spectrum (or the J-coupling patterns), a large receptive field is needed. The DNNs used in WNN (similar to FID-Net architecture [25]) are based on the WaveNet architecture, which was originally developed for the analysis of long audio signals in the time domain [30]. Due to the dilated convolution layers, WaveNet network effectively observes the audio signal in a wide receptive field. WNN differs from WaveNet and FID-Net in that it works with spectrum in the frequency domain and contains several DNNs with correction steps between them. Similarly to WaveNet architecture, WNN has wide receptive field and perceives the whole NUS spectrum and the entire PSF patterns. The dilated convolutional layers skip a defined number of points in the data and thus can be considered as convolutional layers with gaps. With different dilation sizes for different convolutional layers, it is possible to build a block that behaves like a convolutional layer with a very large kernel size. The use of the dilated convolutional layers is the only feature in common between the WNN and WaveNet (e.g. FID-Net) architectures. There are many significant technical differences between the two. Specifically, WaveNet is designed to be a forward audio generative model, maintaining the temporal order of the data and predicting outputs based only on the preceding values. This requires the use of causal padding in convolutional layers. In contrast, the WNN model captures the entire spectrum by simultaneously looking both forward and backward. Therefore, the WNN layers do not contain padding and shrink at each layer by the dilation rate. In order to have the same output size as the input data, the circling feature of the frequency domain WNN uses two copies of the input data. Fig. 2b illustrates this specific DNN architecture (see Appendix B for python code). Furthermore, while the WNN employs the Rectified Linear Unit (ReLU) activation functions [35] (Fig. 2b), the WaveNet and FID-Net utilize gated activation units [36]. Finally, unlike WaveNet and FID-Net, WNN does not have residual or parameterized skip connections [37].

The presented design of the network requires an input spectrum consisting of $2^n - 1$ points (Fig. 2b, gray circles in the input layer) that after the repetition (white circles in the input layer) form the input layer with $n - 1$ hidden layers. Considering that size of the spectrum can be adjusted by the zero filling, the specific input size required by the DNN does not pose a limitation. Here, we used 2^{m-1} dilation rate for the m-th layer and 20 filters and 2×1 kernel size for each layer, with the ReLU activation functions between the layers.

As described above, a sliding window consisting of three 1D spectra corresponding to three adjacent points along the direct dimension are processed together by WNN. These spectra represent three intertwined channels in DNN. As a result, DNN is trained to reconstruct three adjacent indirect NUS 1D spectra simultaneously based on all three intertwined channels, like RGB channels are used in convolutional neural networks in image processing. Thus, the DNN, the input and output layers have three channels, where the adjacent spectra are simultaneously reconstructed. The adjacent windows overlap by two points and, thus, only the middle channel is used in the final reconstruction.

2.2.2. Normalization

In order to train WNN for NUS reconstruction, K pairs of input (NUS or J-coupled) $[s]^k_{N\times 3}$ and output (US or decoupled) $[S]^k_{N\times 3}$ are formed. Where, $k = 1, 2, \ldots, K$ and each pair is composed of the three channels of the adjacent spectra. For each DNN in the WNN, both input and output are normalized using the maximum Euclidean norm value from the three channels.

2.2.3. Correction step

WNN design (Fig. 2a) contains several DNNs (Fig. 2b) which optimal number depends on the NUS fraction. Each DNN in the WNN architecture is trained independently one after another and as input takes result from the pre-trained upstream network. Thus, the resulting spectrum monotonously improves with more networks in the chain. The initial spectrum S_{NUS}containing strong aliasing artifacts feeds the first DNN, which reduces the artifacts and produces spectrum S_{Pred} more similar to the uniform sampling spectrum. S_{Pred} must be corrected before it is used as an input for the next DNN, as described below. Similarly, Qu et al. [23] previously stated that the FID at the location of sampled data points should be balanced between the acquired data points and the DNN-reconstructed data points. Here we used the following procedure to produce the corrected spectrum S_{Cor}:

$$S_{Cor} = S_{Pred} - S_{Pred} * U + S_{NUS} \tag{6}$$

In the time domain, this correction is equivalent to restoring the experimental data in the FID, while keeping the predicted values for the not sampled points. As schematically shown in Fig. 2a, the correction improves the spectrum. Several consecutive DNN/correction steps are performed to reach good spectrum quality.

As a note, to speed up the calculations, the convolution operation $S_{Pred} * U$ in Eq. (6) is performed in the time domain. Since the DNN deals only with the real part of the spectrum, we use the virtual echo representation [38] to simplify transitions between the frequency and time domains.

2.3. The WNN training

WNNs were trained on the NMRbox server [39] (128 cores 2 TB memory), equipped with 4 NVIDIA A100 TENSOR CORE GPU graphics cards. We generated the network graphs using TensorFlow [40] python package with the Keras frontend (Appendix B), and optimized DNNs within TensorFlow using the stochastic ADAM optimizer [41] with the default parameters and 0.004 learning rate, Huber loss function, mini-batch size equal to 128 and the number of epochs equal to 500 or when a monitored metric has stopped improving on validation data set.

The final training- and cross-validation losses for the second DNN of one of the WNN-F for the medium-sized molecule are shown in Fig. 3. There is almost no difference in the appearance of the learning curves for the other DNNs for all WNNs in different molecule sizes.

2.4. Protein NMR spectra

2.4.1. Samples and experiments

For the NMR experiments, we used the previously described protein samples: U — ^{15}N-^{13}C — labeled Cu(I) azurin (14 kDa)

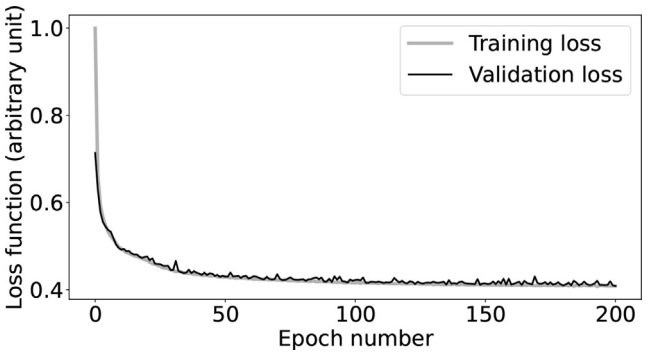

Fig. 3. Training- and cross-validation losses for the second DNN of one of the WNN-F for the medium-sized molecule during training with Loss function: Huber, Mini-batch size: 128, and Total amount of training data: 2^{16} with 20% of the validation data set.

[42], U — ^{15}N-^{13}C — labeled ubiquitin (8.6 kDa) [43], and U — ^{15}-N-^{13}C-^{2}H methyl ILV back-protonated MALT1 (44 kDa) [31,32]. The fully sampled two-dimensional experiments used in this study are described in Table 4.

2.4.2. Processing with compressed sensing and SMILE

We used *NMRPipe* [44], *mddnmr* [3], and python package *nmrglue* [45] for reading, writing, and traditional processing of the NMR spectra. For the NUS processing with WNN, CS-IST, and SMILE, the ^{1}H-^{15}N correlation spectra were down-sampled to the number of NUS points specified in Table 4. CS-IST and CS-virtual decoupling (CS-VD) [46] calculations were performed using default *mddnmr* parameters and the Virtual-Echo [38] mode.

2.4.3. NUS spectra quality metrics

Since the WNN network was trained to reconstruct NUS spectrum with the best point-to-point match to the Fourier spectrum of the uniformly sampled signal, we use two metrics that assess similarity of the reconstruction with the corresponding fully sampled spectra. These are the point-by-point root-mean-square deviation (*RMSD*) and the correlation coefficients (R_S^2). Before the comparison, all spectra were normalized to their maximal peak intensity. To limit the potential effects of the baseline noise on the quality metrics, *RMSD* and R_S^2 were calculated only for the spectral points with intensities above 1% of the highest peak intensity in either of the two compared spectra. Thus, both metrics are sensitive to false-positive as well as false-negative spectral artifacts. In addition to the point-to-point scores, in Appendix C, we report results on the four NUScon peak-based quality metrics described in [47].

3. Results and discussion

3.1. WNN 2D NUS reconstruction performance

Performance of the WNNs is demonstrated on several ^{1}H-^{15}N correlation spectra of different complexity for the three proteins Ubiquitin (8.6 kDa), Azurin (14 kDa), and MALT1 (44 kDa). We compared the quality of the reconstructed spectra obtained by WNNs trained using three different NUS/PSF schemes: fixed NUS schedule with a defined PSF pattern (WNN-F), and two WNNs trained with varying NUS schedules, *i.e.* Poisson-gap (WNN-P) and flat-random (WNN-R). The results were also compared with the spectra reconstructions using CS-IST and SMILE algorithms, which are representative of the traditional NUS reconstruction techniques implemented in *mddnmr* and *NMRpipe* software respectively.

Fig. 4 shows the reconstruction results for Azurin (results for Ubiquitin and MALT1 are shown in Fig. A.1 and A.2 in Appendix A). It is clear that all five reconstruction methods, *i.e.* WNN-F, WNN-P, WNN-R, CS-IST, and SMILE, are capable of reproducing the spectrum with good and comparable quality using 21 NUS points (16.5%) out of 128 points in the full reference spectrum. Comparison of the spectra quality metric R_S^2 (The insets plots of Fig. 4) reveals that among the three WNNs, the best result was obtained with WNN-F, which demonstrates the clear advantage of the fixed-schedule approach for WNN training. We, therefore, argue that while the WNN-F network is trained to recognize a specific PSF pattern produced by a defined schedule, the other two networks are trained on a multitude of different PSF realizations and thus cannot benefit from a "familiar" PSF pattern.

Fig. 5 shows point-to-point RMSD and R_S^2 for the Ubiquitin, Azurin, and MALT1 proteins systems, which we obtained using 11, 21, and 31 NUS points out of 128, respectively. In addition to the average, the error bars show the spread of values over 11 different sampling schedules. With its higher R_S^2, lower RMSD, and smaller spreads of these values, the WNN-F displays significantly and consistently better results compared to the other WNN schemes, CS-IST, and SMILE. This result is also consistent with the peak-based NUScon metrics shown in Fig. C.3 and Fig. C.4 in Appendix C. The advantage of the WNN-F scheme is the most pronounced for the low NUS fraction. We hypothesize that at the low NUS, the PSF aliasing artifacts are the strongest and constitute an easily detectable pattern for WNN-F. In contrast, at the higher NUS rate, intensities of the artifact peaks relative to the true/main peak are reduced, which reduces the value of the PSF pattern recognition and thus, diminishes the differences between the different WNN training schemes. The noticeable advantage of the WNN-P results over the WNN-R is consistent with previous observations [48]. It is also noteworthy that although CS-IST and SMILE produce reconstructions of similar average quality to WNN-P and WNN-R, these methods show a higher spread of the point-to-point and/or peak-based scores, which indicates a larger depen-

Table 4
Spectral parameters.

Protein	Size (kDa)	Concentration (mM)	Spectrum	Spectral width (Hz)	All points	NUS points
Ubiquitin	8.6	0.6	^{1}H-^{15}N — HSQC	3648.8	128	11
Azurin	14	1.0	^{1}H-^{15}N — HSQC	3648.8	128	21
MALT1	44	0.5	^{1}H-^{15}N — TROSY	3283.9	128	31
			^{1}H-^{13}C — HMQC	4300.5	200	-
			^{1}H-^{13}C — CT-HMQC	4526.8	100	-

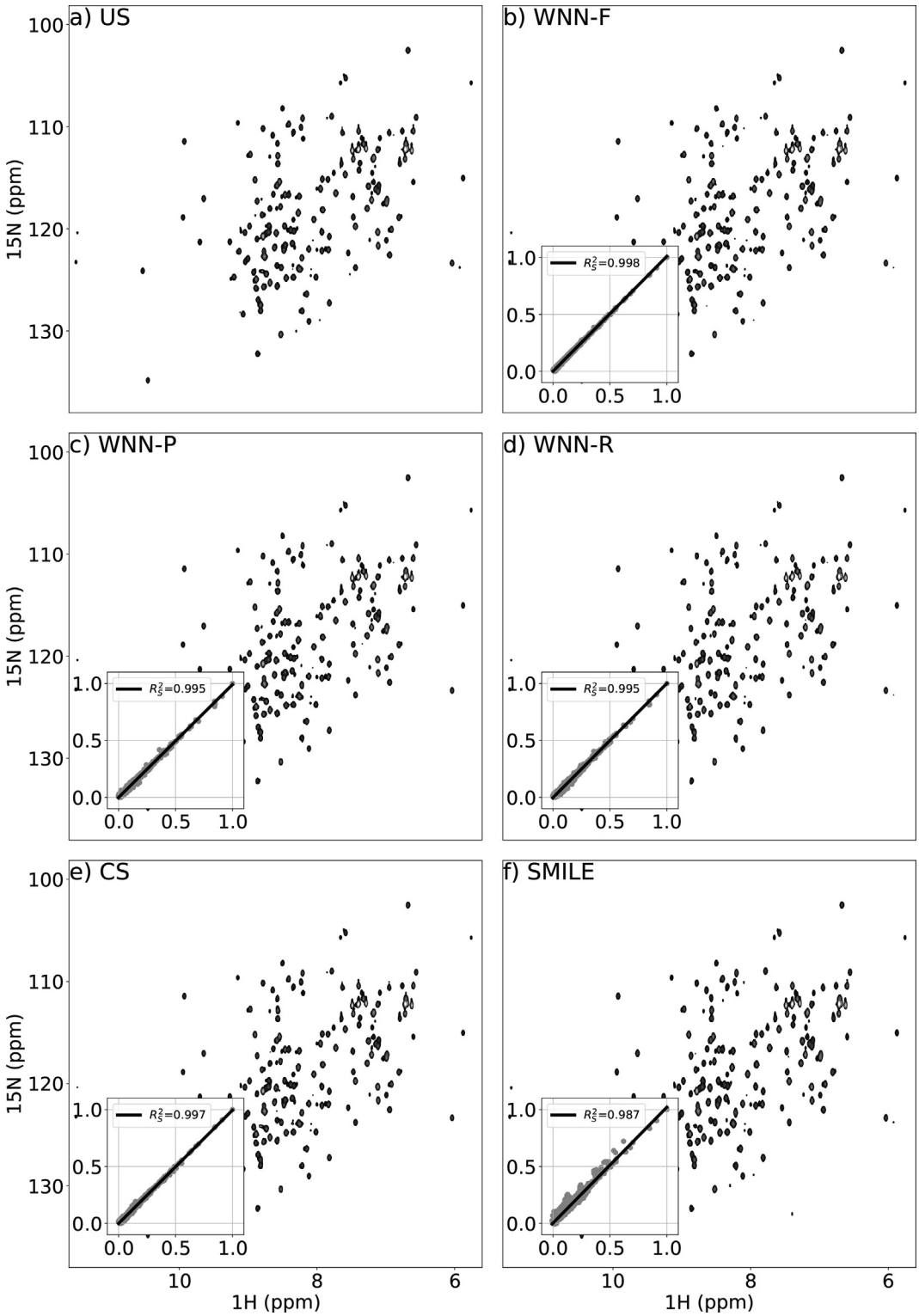

Fig. 4. 2D ^{1}H-^{15}N — HSQC spectra of Azurin. (a) Uniformly Sampled (US) spectrum, (b-f) Spectra reconstructed with WNN-F, WNN-P, WNN-R, CS-IST, and SMILE, respectively. The insets show intensity correlations between the US and reconstructed spectra.

dence of the results on the selected sampling schedule, especially at low NUS levels.

3.2. R^2 and the number of WNNs

As explained in the Method section and displayed in Fig. 2, WNN consists of several nested DNNs which gradually improve the quality of the reconstructed spectrum. To reduce the amount of computations at the WNN training and spectra reconstruction stages, the number of DNNs should be small. Fig. 6 presents statistics obtained on the 1500 synthetic test spectra corresponding to small, medium, and large proteins (see Section 2.1.3). We measured average R_S^2 between 1500 uniform sampling synthetic spectra and the corresponding WNN-F reconstructed NUS spectra for

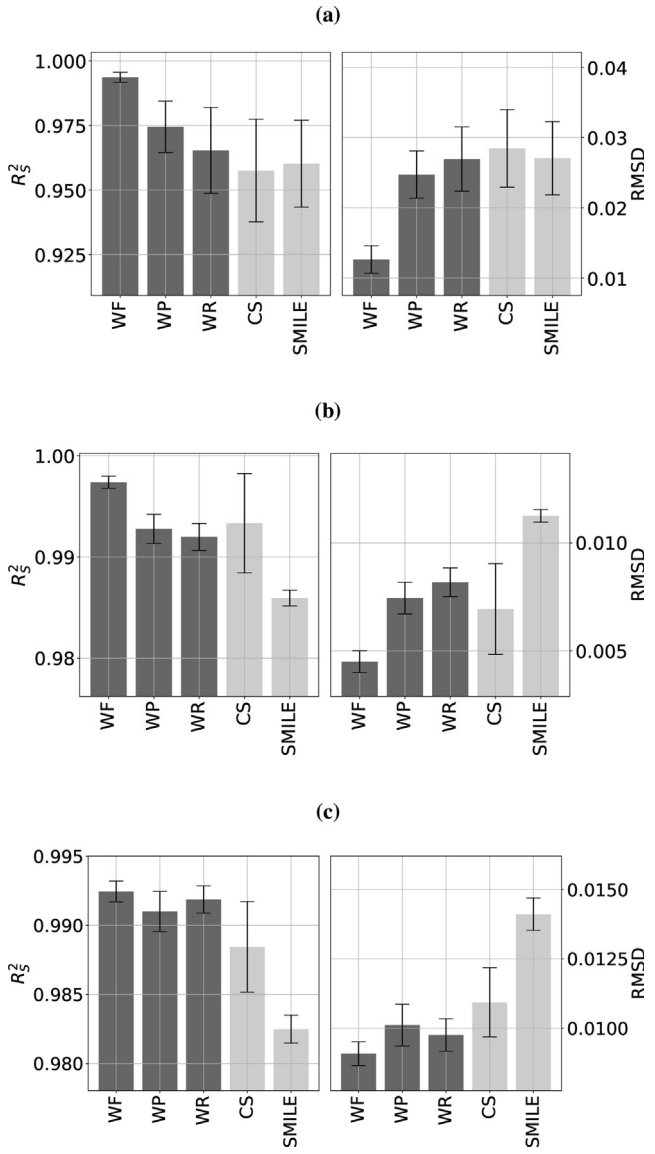

Fig. 5. Mean (bar graphs) and STD (error bar) of the signal intensity RMSD and correlation coefficients (R_S^2) between the normalized uniformly sampled and reconstructed NUS spectra using WNN trained with fixed (WNN-F), unfixed Poisson-Gap (WNN-P), and unfixed random (WNN-R) sampling, CS-IST (CS) and SMILE (see Methods for details) (a) Ubiquitin spectra with an 11 out of 128 Poisson-gap sampling; (b) Azurin spectra with a 21 out of 128 Poisson-gap sampling; (c) MALT spectra with a 31 out of 128 Poisson-gap sampling.

small (gray open squares), medium (black squares in both panels), and large (gray small squares) proteins with 11, 21, and 31 NUS points out of 128 respectively. Also, for medium proteins, in addition to WNN-F reconstructed spectra (black squares), we show R_S^2 results for WNN-P (black circles) and WNN-R (black triangles) reconstructions. The spread of the scores, which are shown as error bars, was obtained by repeating the calculations for 11 different NUS sampling schemes using the correspondingly trained WNN-Fs. The optimal number of DNNs, *i.e.* when the quality of the spectra does not improve with additional DNNs, depends primarily on the type of the sampling scheme. Namely, the WNN-F curves (black squares) for 21 NUS points out of 128 show clear signs of leveling off at 6 DNNs, whereas WNN-P (black circles) and WNN-R (black triangles) require at least 15 DNNs. Furthermore, a comparison of the curves for the WNN-F at NUS levels 31/128 (gray small

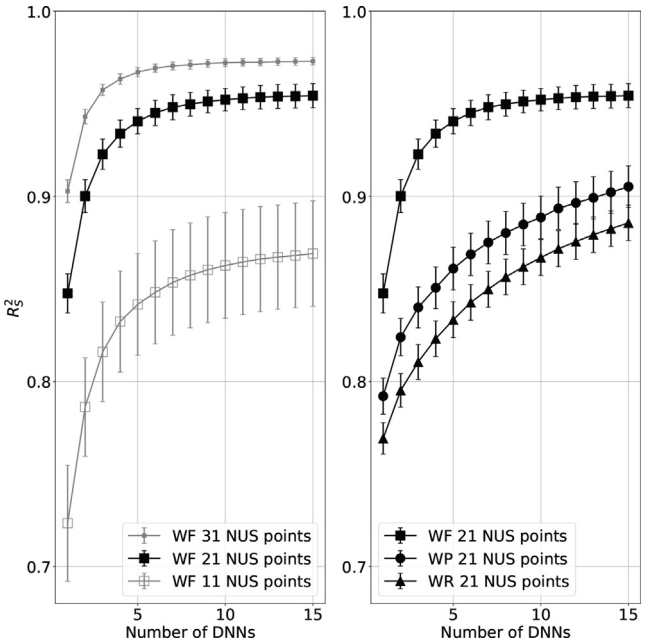

Fig. 6. Mean and STD (error bar) versus the number of DNNs in the WNN structure for the average signal intensity correlations R^2 between 1500×11 uniformly sampled synthetic spectra and corresponding reconstructed spectra using WNN-F (black squares in both panels), WNN-P (black circles) and WNN-R (black triangles) corresponding to a medium size protein spectrum with 21 points out of 128 NUS. (gray small squares) and (gray open squares) - the results for WNN-F for small and large proteins with 11 and 31 NUS points out of 128, respectively.

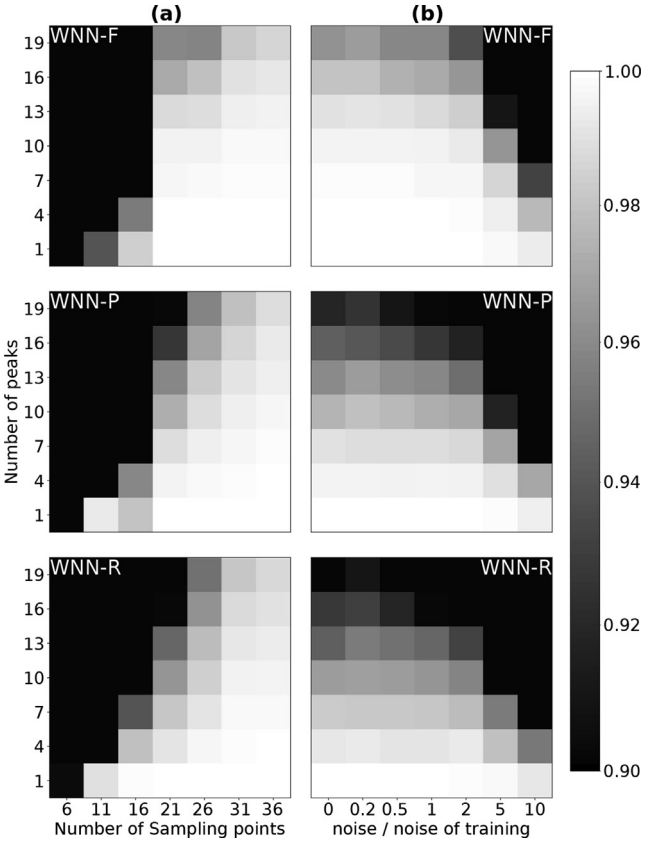

Fig. 7. Performance of the WNN NUS reconstruction (a) beyond the NUS schedule density used for the network training (i.e. 21 out of 128 sampling points) and (b) versus noise amplitude different from the level used in the training. The average signal intensity correlations (R_S^2) between the reference uniform sampling synthetic spectra and their corresponding reconstructed spectra using WNN-F, WNN-P, and WNN-R for a medium-size protein (See Methods for details).

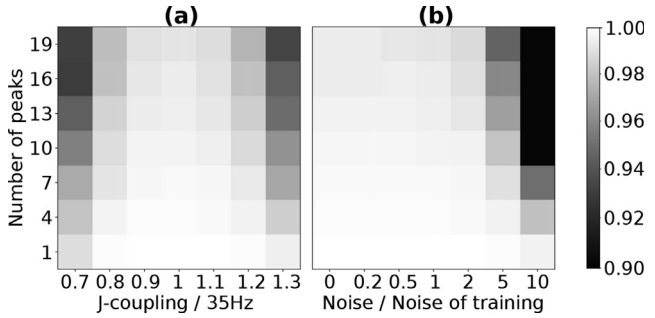

Fig. 8. Performance of the WNN-decoupling (a) for the J-coupling values deviating from 35 Hz used in the training and (b) beyond the training noise level. (See Methods for details). By the gray scale level shown the average signal intensity correlations (R_S^2) between the reference decoupled synthetic spectra and the corresponding spectra reconstructions using the WNN virtual decoupling.

squares), 21/128 (black squares), and 11/128 (gray open squares) show that fewer networks are needed for higher NUS fraction.

3.3. WNN Robustness vs altered NUS schedule size and noise level

All the WNNs were trained with defined NUS fractions, *i.e.* 11, 21, 31 points out of 128 with added the Gaussian noise to emulate the noise presented in realistic NMR spectra. However, in practical experiments, it is often needed to adjust the number of points, for example, to add more points to fit a spectrometer time allocation or to process an old experiment or an experiment that finished prematurely with fewer points. In these cases, the problem can be solved, although with relatively high computational costs, by training a new WNN with the actually needed NUS schedule. Fig. 7-a illustrates an alternative approach by showing performance of the WNN-F, WNN-P, and WNN-R beyond

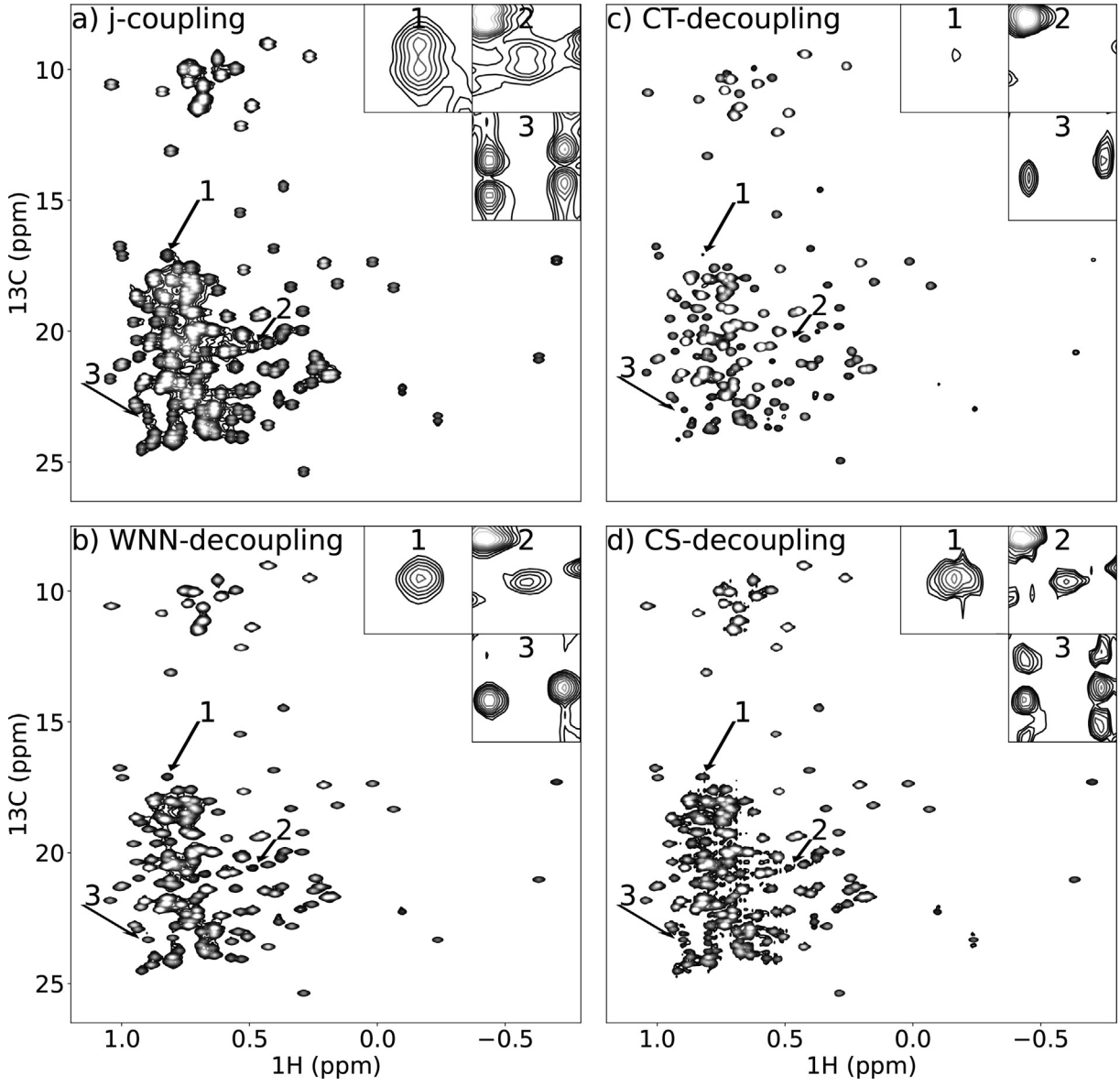

Fig. 9. High resolution methyl 2D ^{1}H-^{13}C — HMQC spectra of protein MALT1. Each spectrum is normalized and plotted at the same contour level with only positive contours shown. (a) Spectrum without decoupling processed with Fourier transform. (b) Spectrum decoupled using WNN-F. (c) Constant time ^{1}H-^{13}C — HMQC spectrum. (d) Spectrum decoupled by deconvolution using the CS algorithm.

their training schedules size of 21 points. An altered schedule is produced by either truncating the NUS table or by augmenting its size with additional random points. Thereafter, corresponding test spectra were simulated (see Section 2.1.3). All WNN's types produce better R_S^2 scores with more points than in the training data. WNN-F shows the best result for 21 points and 26, when it can reliably reproduce spectra with up to 19 peaks. With 31 and 36 points, R_S^2 scores are even better, although the values for all WNNs are more similar. For all WNNs, the scores drop sharply when less than 21 NUS points are used for the spectra reconstruction. This indicates that 21 points represents the lower borderline for successful reconstruction. The comparatively lower score for WNN-F when using less than 21 NUS points may be explained by fast degradation of the specific PSF pattern when points are removed from the schedule. These results demonstrate that all WNNs can be used with more NUS points than for their training, but reconstructions with fewer points should be performed with caution. Fig. 7-b illustrates the performance of the WNN-F, WNN-P, and WNN-R beyond the training noise level for the medium-size protein spectrum with 21 points out of 128 NUS. The results show higher performance and more robustness of WNN-F than WNN-P and WNN-R in different noise levels.

The simulations confirm the result presented for the real spectra in Figs. 4, 5, A.1, and A.2 that show significantly higher quality spectra reconstructions by WNN-F compared to the other processing schemes. For the WNNs, this is easily rationalized since a network obviously benefits from training on exactly the same PSF as it is used in the presented experiment. In the broader context, SMILE, CS-IST, WNN-P, and WNN-R, which do not take advantage of prior knowledge about the PSF, display similar performances. The use of a fixed NUS schedule may be considered as a lack of flexibility and thus a disadvantage [24,25]. However, in a recent study, it has been shown that some sampling schedules from a defined random distribution, e.g. Poisson-gap, yield better results than others [49], thus, advocating the use of fixed preselected schedules. Based on our results, we hypothesized that WNN-F's ability to outperform the other methods is due to the use of PSF as new, so far untapped, prior knowledge for successful spectra reconstruction.

3.4. Virtual decoupling by WNN

Similar to PSF, the WNN architecture can be trained to recognize other patterns in the spectra. The obvious examples are peak multiplets caused by scalar coupling. In this work, we demonstrate virtual homo decoupling in methyl 2D ^{1}H-^{13}C — HMQC spectrum of 44 kDa protein MALT1 (Fig. 9). Without the decoupling (Fig. 9a), the ^{13}C resonances are split due to approximately 35 Hz J-coupling with the adjacent methyl ^{13}C atom. This drastically reduces the spectral resolution. In the experiment, the peak splitting can be suppressed by using constant-time (CT) evolution, albeit with the price of significant loss of sensitivity, especially for large molecular systems. Effects of the CT decoupling are illustrated in Fig. 9c. Notably, peaks enlarged in insets 1–3 are narrowed at the expense of significant attenuation and even loss of the peaks as shown in insets 1 and 2.

The virtual decoupling (VD) may solve the sensitivity problem (Fig. 9b,d). Furthermore, VD allows for higher flexibility in choosing the acquisition time than CT and, thus may offer a higher practical spectral resolution. However, VD using traditional algorithmic techniques [46,50–53] as exemplified by CS-IST in Fig. 9d have a caveat in the necessity to provide the algorithm with nearly exact value of the coupling constant. Two peaks shown in insets 3 in Fig. 9 have J-coupling of 41 Hz, which is larger than the value (35 Hz) used for the whole spectrum. As a result, peaks in inset 3 in Fig. 9d are corrupted. Our WNN was trained for a range of J-coupling values and thus demonstrates excellent virtual decoupling (Fig. 9b in real data and Fig. 8 in synthetic data) with both high sensitivity and tolerance to the dispersion of the J-coupling values. Although the excellent pattern recognition ability of DNN has been utilized for the VD [24,29], our results point to the fundamental similarity of the problems of the VD and spectral reconstruction from NUS data. In both cases, known patterns of the spectral features, *i.e.* PSF and peak multiplets, can be used as valuable prior knowledge to successfully reconstruct the spectrum.

4. Conclusion

We present a new DNN-based architecture WNN, which is specifically designed to grasp patterns over the entire NMR spectrum. If trained at a fixed NUS schedule, the WNN benefits from pattern recognition of the corresponding PSF pattern produced by each peak, which allows the highest quality and robust reconstruction of the NUS spectra. As another example of the pattern recognition by WNN, we demonstrate virtual decoupling in 2D methyl ^{1}H-^{13}C — HMQC spectrum of 44 kDa protein MALT1. As far as we know, WNN is the first tool that specifically uses PSF as prior knowledge in NUS spectra reconstruction. WNN demonstrates that the pattern-oriented signal processing schemes may be very efficient and surpass the existing algorithmic methods developed for the reconstruction of NUS spectra, which do not fully exploit the knowledge about the NUS schedule.

Ethical approval

The work does not concern any ethical issues and did not involve any subjetcs.

Consent for publication

All authors gave their consent for the publication.

Declaration of Competing Interest

The authors declare that they have no known competing financial interests or personal relationships that could have appeared to influence the work reported in this paper.

Acknowledgement

The work was supported by the Swedish Foundation for Strategic Research grant ITM17-0218 to T.A and P.A., grant RSF 19-74-30014 to D.L., Swedish Cancer Society grant 21 1605 Pj01H to A. A., and the Swedish Research Council grants 2021–05061 to A.A. and 2019–03561 to V.O. This study used NMRbox: National Center for Biomolecular NMR Data Processing and Analysis, a Biomedical Technology Research Resource (BTRR), which is supported by NIH grant P41GM111135 (NIGMS).

Appendix A

See Figs. A.1 and A.2.

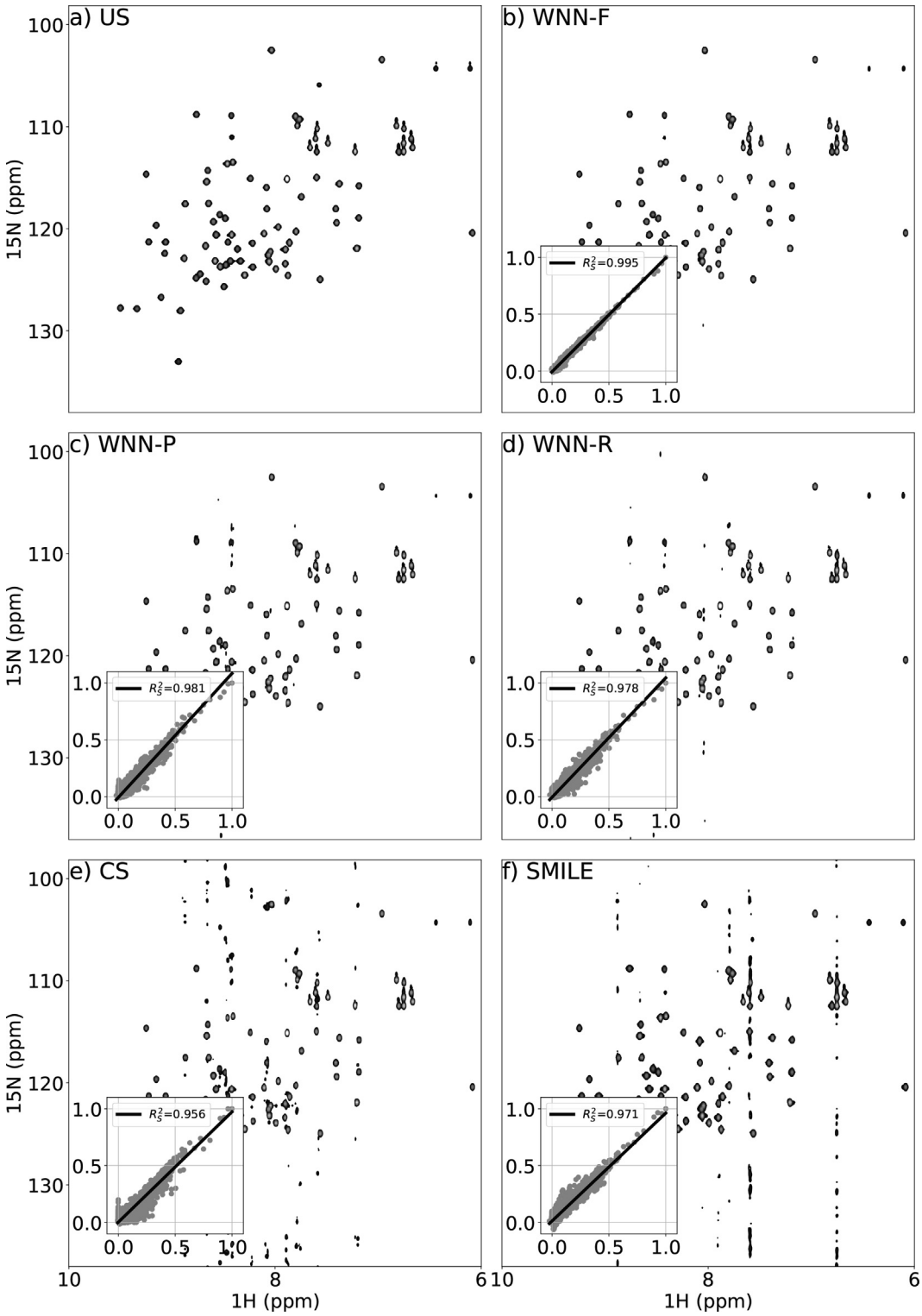

Fig. A.1. 2D ^{1}H-^{15}N — HSQC spectra of Ubiquitin. (a) Uniformly Sampled (US) spectrum, (b-f) Spectra reconstructed with WNN-F, WNN-P, WNN-R, CS-IST, and SMILE, respectively. The insets show intensity correlations between the US and reconstructed spectra.

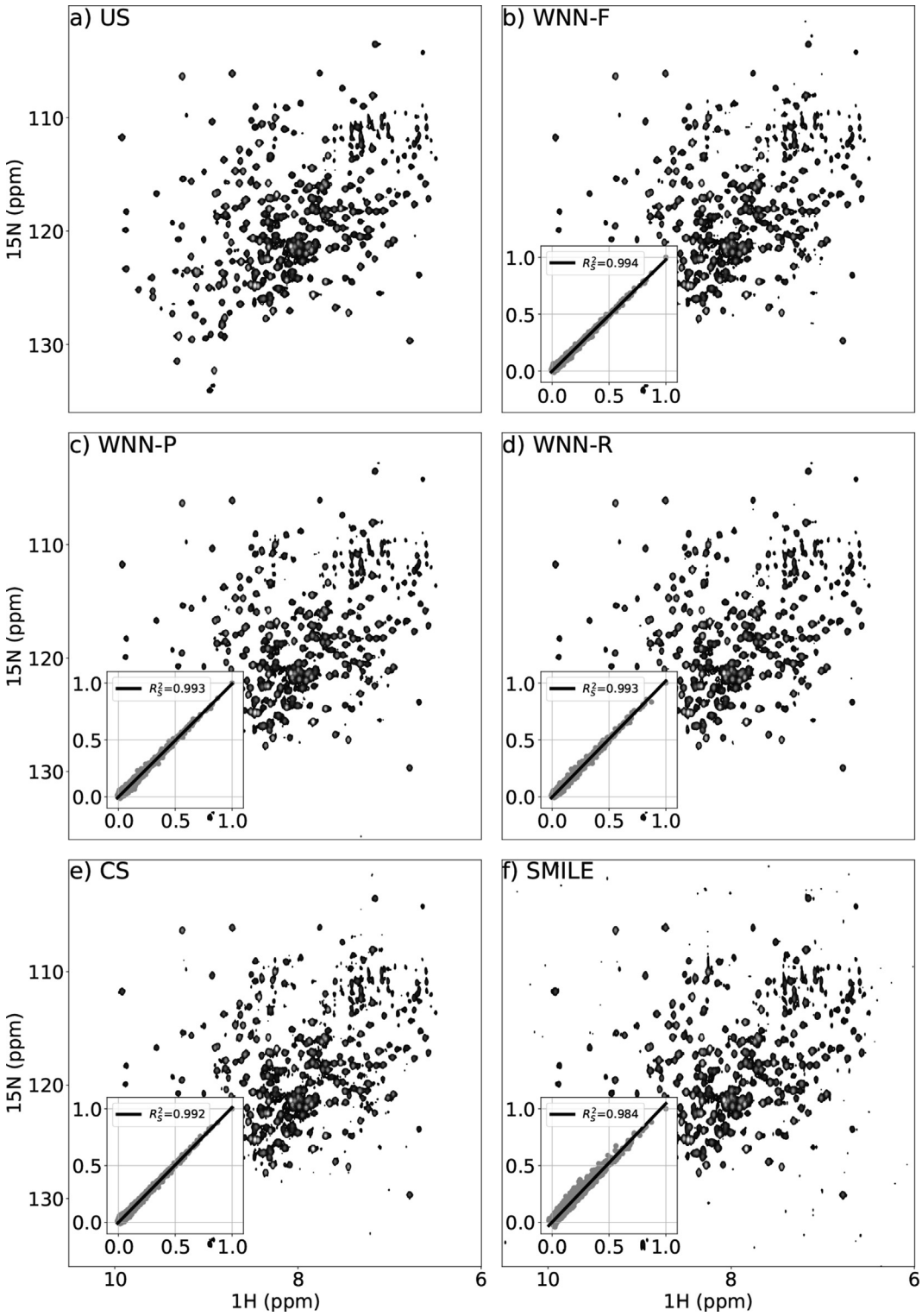

Fig. A.2. 2D ^{1}H-^{15}N — TROSY spectra of MALT1. (a) Uniformly Sampled (US) spectrum, (b-f) Spectra reconstructed with WNN-F, WNN-P, WNN-R, CS-IST, and SMILE, respectively. The insets show intensity correlations between the US and reconstructed spectra.

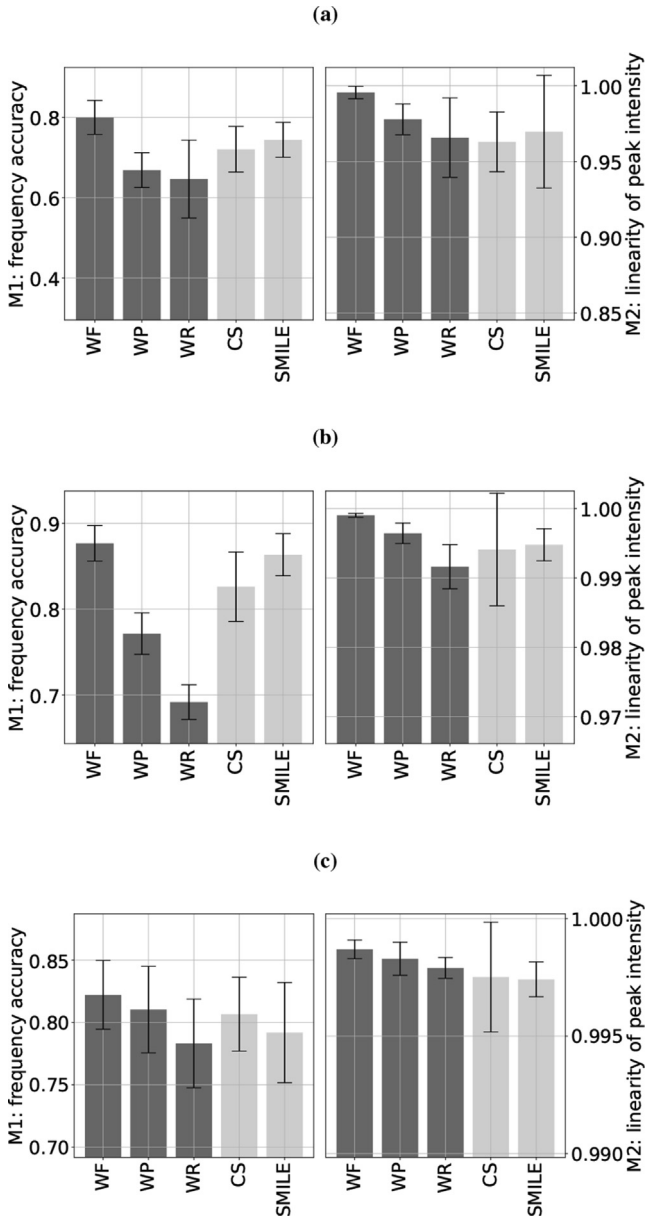

Fig. C.3. Mean (bar graphs) and STD (error bar) of M1: frequency accuracy and M2: the linearity of peak intensity between the normalized uniformly sampled and reconstructed NUS spectra using WNN trained with fixed (WNN-F), unfixed Poisson-Gap (WNN-P), and unfixed random (WNN-R) sampling, CS-IST (CS) and SMILE (see Methods for details) for selected peaks without overlaps (a) Ubiquitin spectra with an 11 out of 128 Poisson-gap sampling; (b) Azurin spectra with a 21 out of 128 Poisson-gap sampling; (c) MALT spectra with a 31 out of 128 Poisson-gap sampling.

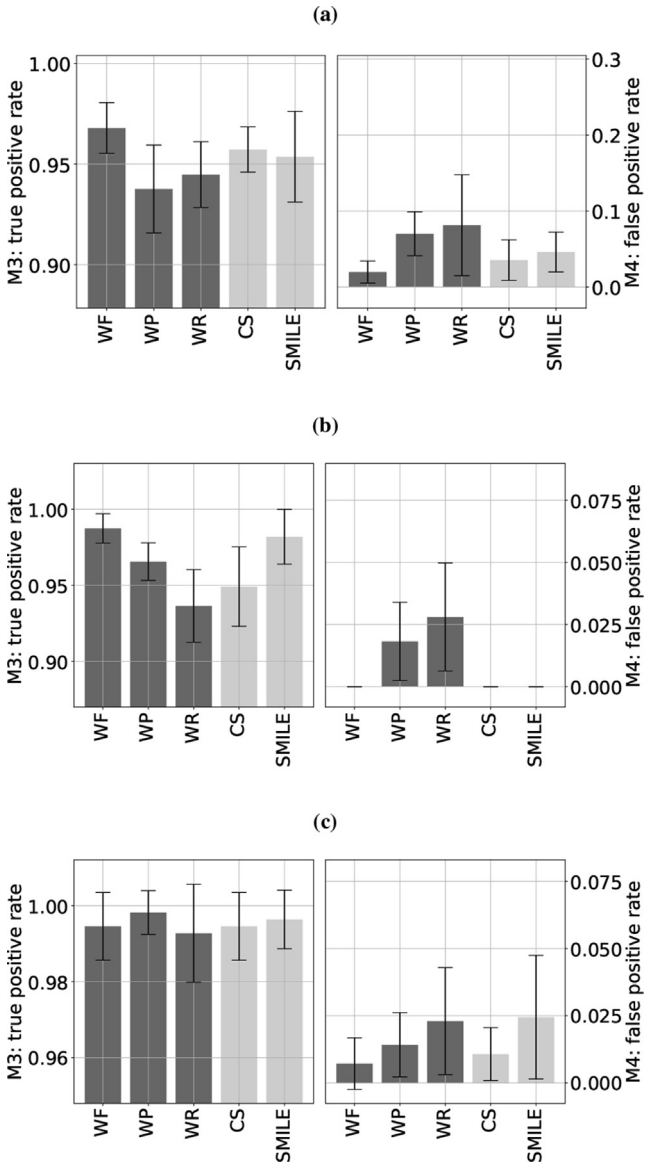

Fig. C.4. Mean (bar graphs) and STD (error bar) of M3: true positive rate and M4: false positive rate between the normalized uniformly sampled and reconstructed NUS spectra using WNN trained with fixed (WNN-F), unfixed Poisson-Gap (WNN-P), and unfixed random (WNN-R) sampling, CS-IST (CS) and SMILE (see Methods for details) for selected peaks without overlaps (a) Ubiquitin spectra with an 11 out of 128 Poisson-gap sampling; (b) Azurin spectra with a 21 out of 128 Poisson-gap sampling; (c) MALT spectra with a 31 out of 128 Poisson-gap sampling.

Appendix B. Python code for building DNNs of WNN

```
import tensorflow as tf
import numpy as np
def WNN(Number_of_point,sliding_window):
    input = tf.keras.layers.Input(shape =
  [2*Number_of_point-1, sliding_window])
    x = tf.concat([input, input], 1)
    x = tf.keras.layers.Reshape((x.shape[1],1,x.sha
  pe[2]))(x)
    for dil in range(int(np.log2(Number_of_point))
  +1):
        x = tf.keras.layers.Conv2D(filters = 20,
  kernel_size = (2,1), dilation_rate = (2**dil,1))
  (x)
        x = tf.keras.activations.relu(x, alpha = 0.2)
    x = tf.keras.layers.Conv2D(filters = slid-
  ing_window, kernel_size = (1,1))(x)
    output = tf.keras.layers.Reshape((2*Number_o-
  f_point-1, sliding_window))(x)
    model = tf.keras.Model(inputs = input,
  outputs = output) model.compile(loss = tf.keras.
  losses.Huber(), optimizer = tf.keras.optimizers.
  Adam(learning_rate = 0.004))
    return model
```

The trained WNNs and ready-to-use examples presented in the paper are available at NMRbox.org.

Appendix C. NUScon based matrics

For robust analysis of the WNN reconstruction algorithm based on NUScon metrics, we select 50 peaks with intensities between 0.04 and 1 from a normalized uniform sampled spectrum for each Ubiquitin, Azurin, and MALT protein that do not overlap with any other peaks. The NMRpipe peak picker then generates a master peak list (M) of 50 selected peaks from fully sampled data for each protein.

Then, 11 recover peak lists (R) are generated by NMRPipe peak picker with the same parameters from the region 3 times the linewidth away from each of the selected 50 peaks in normalized reconstructed spectra using WNN-F, WNN-P, WNN-R, CS-IST, and SMILE for 11 different NUS schemes.

For assessing reconstruction fidelity, we use the following NUScon-based metrics (see NUScon Appendix A [47] for more details):

- M1: frequency accuracy
- M2: linearity of peak intensity
- M3: true positive rate
- M4: false positive rate

References

[1] T.D. Claridge, High-resolution NMR Techniques in Organic Chemistry, vol. 27, Elsevier, 2016.
[2] J. Cavanagh, W.J. Fairbrother, A.G. Palmer III, N.J. Skelton, Protein NMR Spectroscopy: Principles and Practice, Academic Press, 1996.
[3] V. Jaravine, I. Ibragimov, V. Orekhov, Removal of a time barrier for high-resolution multidimensional nmr spectroscopy, Nature Methods 3 (2006) 605–607, https://doi.org/10.1038/nmeth900.
[4] M. Mobli, J.C. Hoch, Nonuniform sampling and non-fourier signal processing methods in multidimensional nmr, Prog. Nucl. Magn. Reson. Spectrosc. 83 (2014) 21–41, https://doi.org/10.1016/j.pnmrs.2014.09.002.
[5] X. Qu, M. Mayzel, J.-F. Cai, Z. Chen, V. Orekhov, Accelerated nmr spectroscopy with low-rank reconstruction, Angew. Chem. Int. Ed. 127 (2014), https://doi.org/10.1002/ange.201409291.
[6] K. Kazimierczuk, V. Orekhov, Accelerated nmr spectroscopy by using compressed sensing, Angew. Chem.(Int. ed. in English) 50 (2011) 5556–5559, https://doi.org/10.1002/anie.201100370.
[7] S. Hyberts, A. Milbradt, A. Wagner, H. Arthanari, G. Wagner, Application of iterative soft thresholding for fast reconstruction of nmr data non-uniformly sampled with multidimensional poisson gap scheduling, J. Biomol. NMR 52 (2012) 315–327, https://doi.org/10.1007/s10858-012-9611-z.
[8] H. Hassanieh, M. Mayzel, L. Shi, D. Katabi, V. Orekhov, Fast multi-dimensional nmr acquisition and processing using the sparse fft, J. Biomol. NMR 63 (2015), https://doi.org/10.1007/s10858-015-9952-5.
[9] S. Hyberts, K. Takeuchi, G. Wagner, Poisson-gap sampling and forward maximum entropy reconstruction for enhancing the resolution and sensitivity of protein nmr data, J. Am. Chem. Soc. 132 (2010) 2145–2147, https://doi.org/10.1021/ja908004w.
[10] Y. Pustovalova, M. Mayzel, V. Orekhov, Extra-large nmr spectroscopy (xlsy), Angew. Chem. Int. Ed. English 130 (2018), https://doi.org/10.1002/ange.201806144.
[11] S. Sibisi, J. Skilling, R.G. Brereton, E.D. Laue, J. Staunton, Maximum entropy signal processing in practical nmr spectroscopy, Nature 311 (5985) (1984) 446–447.
[12] I. Drori, Fast minimization by iterative thresholding for multidimensional nmr spectroscopy, EURASIP J. Adv. Signal Process. 2007 (2007) 1–10.
[13] D.J. Holland, M.J. Bostock, L.F. Gladden, D. Nietlispach, Fast multidimensional nmr spectroscopy using compressed sensing, Angew. Chem. 123 (29) (2011) 6678–6681.
[14] B. Jiang, X. Jiang, N. Xiao, X. Zhang, L. Jiang, X. an Mao, M. Liu, Gridding and fast fourier transformation on non-uniformly sparse sampled multidimensional NMR data, J. Magn. Reson. 204 (1) (2010) 165–168, https://doi.org/10.1016/j.jmr.2010.02.009.
[15] J. Ying, F. Delaglio, D.A. Torchia, A. Bax, Sparse multidimensional iterative lineshape-enhanced (smile) reconstruction of both non-uniformly sampled and conventional NMR data, J. Biomol. NMR 68 (2017) 101–118.
[16] C. Reilly, B. Kowalski, Nuclear magnetic resonance spectral interpretation by pattern recognition, J. Phys. Chem. 75 (10) (1971) 1402–1411.
[17] D. Chen, Z. Wang, D. Guo, V. Orekhov, X. Qu, Review and prospect: Deep learning in nuclear magnetic resonance spectroscopy, Chem.– A Eur. J. 26 (46) (2020) 10391–10401, https://doi.org/10.1002/chem.202000246, arXiv: https://chemistry-europe.onlinelibrary.wiley.com/doi/pdf/10.1002/chem.202000246.
[18] H. Lee, H. Kim, Intact metabolite spectrum mining by deep learning in proton magnetic resonance spectroscopy of the brain, Magn. Reson. Med. (2019), https://doi.org/10.1002/mrm.27727.
[19] S. Liu, J. Li, K. Bennett, B. Ganoe, T. Neudecker, M. Head-Gordon, A. Hexemer, D. Ushizima, T. Head-Gordon, A multi-resolution 3d-densenet for chemical shift prediction in nmr crystallography, J. Phys. Chem. Lett. 10 (2019), https://doi.org/10.1021/acs.jpclett.9b01570.
[20] P. Klukowski, M. Augoff, M. Zieba, M. Drwal, A. Gonczarek, M. Walczak, Nmrnet: A deep learning approach to automated peak picking of protein nmr spectra, Bioinformat. (Oxford, England) 34 (2018), https://doi.org/10.1093/bioinformatics/bty134.
[21] D.-W. Li, A.L. Hansen, L. Bruschweiler-Li, C. Yuan, R. Brüschweiler, Fundamental and practical aspects of machine learning for the peak picking of biomolecular NMR spectra, J. Biomol. NMR (2022) 1–9.
[22] P. Klukowski, R. Riek, P. Güntert, Leveraging deep learning for fully automated nmr protein structure determination, arXiv preprint arXiv:2201.12041 (2022).
[23] X. Qu, Y. Huang, H. Lu, T. Qiu, D. Guo, T. Agback, V. Orekhov, Z. Chen, Accelerated nuclear magnetic resonance spectroscopy with deep learning, Angew. Chem. 132 (26) (2020) 10383–10386.
[24] D. Hansen, Using deep neural networks to reconstruct non-uniformly sampled NMR spectra, J. Biomol. NMR 73 (2019), https://doi.org/10.1007/s10858-019-00265-1.
[25] G. Karunanithy, D. Hansen, Fid-net: A versatile deep neural network architecture for nmr spectral reconstruction and virtual decoupling, J. Biomol. NMR 75 (2021), https://doi.org/10.1007/s10858-021-00366-w.
[26] J. Luo, Q. Zeng, K. Wu, Y. Lin, Fast reconstruction of non-uniform sampling multidimensional nmr spectroscopy via a deep neural network, J. Magn. Reson. 317 (2020) 106772, https://doi.org/10.1016/j.jmr.2020.106772.
[27] J.L. Amey, J. Keeley, T. Choudhury, I. Kuprov, Neural network interpretation using descrambler groups, Proc. Nat. Acad. Sci. 118 (5) (2021), e2016917118.
[28] C. Bishop, Pattern Recognition and Machine Learning (Information Science and Statistics), Springer, New York, NY, 2007.
[29] G. Karunanithy, H.W. Mackenzie, D.F. Hansen, Virtual homonuclear decoupling in direct detection nuclear magnetic resonance experiments using deep neural networks, J. Am. Chem. Soc. 143 (41) (2021) 16935–16942.
[30] A.V.d. Oord, S. Dieleman, H. Zen, K. Simonyan, O. Vinyals, A. Graves, N. Kalchbrenner, A. Senior, K. Kavukcuoglu, Wavenet: A generative model for raw audio (2016). https://doi.org/10.48550/ARXIV.1609.03499. https://arxiv.org/abs/1609.03499.

[31] S. Unnerståle, M. Nowakowski, V. Baraznenok, G. Stenberg, J. Lindberg, M. Mayzel, V. Orekhov, T. Agback, Backbone assignment of the malt1 paracaspase by solution NMR, Plos One 11 (1) (2016) e0146496.
[32] X. Han, M. Levkovets, D. Lesovoy, R. Sun, J. Wallerstein, T. Sandalova, T. Agback, A. Achour, P. Agback, Y. Orekhov, Vladislav, Assignment of ivl-methyl side chain of the ligand-free monomeric human malt1 paracaspase-igl 3 domain in solution, Res. Square (2022), https://doi.org/10.21203/rs.3.rs-1820939/v1.
[33] V.Y. Orekhov, V.A. Jaravine, Analysis of non-uniformly sampled spectra with multi-dimensional decomposition, Progress nucl. Magnetic Reson. Spectrosc. 59 (3) (2011) 271–292.
[34] P. Kasprzak, M. Urbanczyk, K. Kazimierczuk, Clustered sparsity and poisson-gap sampling, J. Biomol. NMR 75 (2021), https://doi.org/10.1007/s10858-021-00385-7.
[35] A.F. Agarap, Deep learning using rectified linear units (relu), arXiv preprint arXiv:1803.08375 (2018).
[36] A. Van den Oord, N. Kalchbrenner, L. Espeholt, O. Vinyals, A. Graves, et al., Conditional image generation with pixelcnn decoders, Adv. Neural Informat. Process. Syst. 29 (2016).
[37] K. He, X. Zhang, S. Ren, J. Sun, Deep residual learning for image recognition, in: Proceedings of the IEEE Conference on Computer Vision and Pattern Recognition, 2016, pp. 770–778.
[38] M. Mayzel, K. Kazimierczuk, V. Orekhov, Causality principle in reconstruction of sparse nmr spectra, Chem. Commun. (Cambridge, England) 50 (2014), https://doi.org/10.1039/c4cc03047h.
[39] M.W. Maciejewski, A.D. Schuyler, M.R. Gryk, I.I. Moraru, P.R. Romero, E.L. Ulrich, H.R. Eghbalnia, M. Livny, F. Delaglio, J.C. Hoch, Nmrbox: A resource for biomolecular nmr computation, Biophys. J. 112 (8) (2017) 1529–1534, https://doi.org/10.1016/j.bpj.2017.03.011.
[40] M. Abadi, A. Agarwal, P. Barham, E. Brevdo, Z. Chen, C. Citro, G.S. Corrado, A. Davis, J. Dean, M. Devin, S. Ghemawat, I. Goodfellow, A. Harp, G. Irving, M. Isard, Y. Jia, R. Jozefowicz, L. Kaiser, M. Kudlur, J. Levenberg, D. Mané, R. Monga, S. Moore, D. Murray, C. Olah, M. Schuster, J. Shlens, B. Steiner, I. Sutskever, K. Talwar, P. Tucker, V. Vanhoucke, V. Vasudevan, F. Viégas, O. Vinyals, P. Warden, M. Wattenberg, M. Wicke, Y. Yu, X. Zheng, TensorFlow: Large-scale machine learning on heterogeneous systems, software available from tensorflow.org (2015). https://www.tensorflow.org/.
[41] D.P. Kingma, J. Ba, Adam: A method for stochastic optimization (2014). arXiv:1412.6980.
[42] D.M. Korzhnev, B.G. Karlsson, V.Y. Orekhov, M. Billeter, Nmr detection of multiple transitions to low-populated states in azurin, Protein Sci. 12 (1) (2003) 56–65.
[43] P.S. Brzovic, A. Lissounov, D.E. Christensen, D.W. Hoyt, R.E. Klevit, A ubch5/ubiquitin noncovalent complex is required for processive brca1-directed ubiquitination, Mol. Cell 21 (6) (2006) 873–880.
[44] F. Delaglio, S. Grzesiek, G.W. Vuister, G. Zhu, J. Pfeifer, A. Bax, Nmrpipe: a multidimensional spectral processing system based on unix pipes, J. Biomol. NMR 6 (3) (1995) 277–293.
[45] J.J. Helmus, C.P. Jaroniec, Nmrglue: an open source python package for the analysis of multidimensional nmr data, J. Biomol. NMR 55 (4) (2013) 355–367.
[46] K. Kazimierczuk, P. Kasprzak, P.S. Georgoulia, I. Matecko-Burmann, B.M. Burmann, L. Isaksson, E. Gustavsson, S. Westenhoff, V.Y. Orekhov, Resolution enhancement in nmr spectra by deconvolution with compressed sensing reconstruction, Chem. Commun. 56 (2020) 14585–14588, https://doi.org/10.1039/D0CC06188C.
[47] Y. Pustovalova, F. Delaglio, D.L. Craft, H. Arthanari, A. Bax, M. Billeter, M.J. Bostock, H. Dashti, D.F. Hansen, S.G. Hyberts, B.A. Johnson, K. Kazimierczuk, H. Lu, M. Maciejewski, T.M. Miljenović, M. Mobli, D. Nietlispach, V. Orekhov, R. Powers, X. Qu, S.A. Robson, D. Rovnyak, G. Wagner, J. Ying, M. Zambrello, J.C. Hoch, D.L. Donoho, A.D. Schuyler, Nuscon: a community-driven platform for quantitative evaluation of nonuniform sampling in NMR, Magnetic Reson. 2 (2) (2021) 843–861, https://doi.org/10.5194/mr-2-843-2021, URL https://mr.copernicus.org/articles/2/843/2021/.
[48] Y. Huang, J. Zhao, Z. Wang, V. Orekhov, D. Guo, X. Qu, Exponential signal reconstruction with deep hankel matrix factorization, IEEE Trans. Neural Networks Learn. Syst. (2021).
[49] S.G. Hyberts, G. Wagner, High fidelity sampling schedules for nmr spectra of high dynamic range, J. Magn. Reson. 339 (2022) 107228, https://doi.org/10.1016/j.jmr.2022.107228.
[50] A. Bothner-By, J. Dadok, Useful manipulations of the free induction decay, J. Magnetic Reson. (1969) 72 (3) (1987) 540–543.
[51] M.A. Delsuc, G.C. Levy, The application of maximum entropy processing to the deconvolution of coupling patterns in nmr, J. Magnetic Reson. (1969) 76 (2) (1988) 306–315.
[52] Z. Serber, C. Richter, D. Moskau, J.-M. Böhlen, T. Gerfin, D. Marek, M. Häberli, L. Baselgia, F. Laukien, A.S. Stern, et al., New carbon-detected protein nmr experiments using cryoprobes, J. Am. Chem. Soc. 122 (14) (2000) 3554–3555.
[53] R. Kerfah, O. Hamelin, J. Boisbouvier, D. Marion, Ch3-specific nmr assignment of alanine, isoleucine, leucine and valine methyl groups in high molecular weight proteins using a single sample, J. Biomol. NMR 63 (4) (2015) 389–402.